

Cite this: *CrystEngComm*, 2013, 15, 8166

Structural evolution and characteristics of the phase transformations between $\alpha\text{-Fe}_2\text{O}_3$, Fe_3O_4 and $\gamma\text{-Fe}_2\text{O}_3$ nanoparticles under reducing and oxidizing atmospheres[†]

Xin Zhang,^a Yongan Niu,^b Xiangdong Meng,^c Yao Li^{*b} and Jiupeng Zhao^{*a}

Received 28th June 2013,
Accepted 5th August 2013

DOI: 10.1039/c3ce41269e

www.rsc.org/crystengcomm

The preparation of high-quality $\alpha\text{-Fe}_2\text{O}_3$, Fe_3O_4 and $\gamma\text{-Fe}_2\text{O}_3$ nanoparticles is of great importance for technologies and applications in drug delivery,^{1,2} functional devices,³ lithium-ion batteries,⁴ and so on. The fabrication of the nanoparticles with a controlled morphology, size and structure is of great importance for certain functions. Monodisperse Fe_3O_4 and $\gamma\text{-Fe}_2\text{O}_3$ nanoparticles deserve our special attention due to their high performance parameters, environmentally friendliness and biocompatibility in areas such as biotechnology, ore refining and catalysis.^{5,6} However, it is hard to prepare monodisperse Fe_3O_4 and $\gamma\text{-Fe}_2\text{O}_3$ nanoparticles by the hydrothermal route because the crystal growth of the nanoparticles is prevented by Ostwald ripening,⁷ and the $\gamma\text{-Fe}_2\text{O}_3$ phase appeared to be unstable.⁸ At the same time, the hydrothermal route is a material-saving and highly efficient method of synthesizing monodisperse $\alpha\text{-Fe}_2\text{O}_3$ (hematite) nanoparticles.⁹ Many shapes of $\alpha\text{-Fe}_2\text{O}_3$ nanoparticles have been reported, *i.e.*, spindles,¹⁰ ellipsoids,¹¹ nanotubes,¹² nanowires,¹³ nanocubes,¹⁴ nanorods¹⁵ and snowflakes.¹⁶ Thus, the aim was to transform the $\alpha\text{-Fe}_2\text{O}_3$ phase to the Fe_3O_4 or $\gamma\text{-Fe}_2\text{O}_3$ phase using a green, facile and highly efficient process.

^aHarbin Institute of Technology, School of Chemical Engineering and Technology, Harbin, 150040, P. R. China. E-mail: jiupengzhao@126.com; Fax: +86 451 86403767; Tel: +86 451 86403767

^bCenter for Composite Materials, Harbin Institute of Technology, Harbin, 150040, P. R. China. E-mail: yaoli@hit.edu.cn; Fax: +86 451 86402345; Tel: +86 451 86402345

^cSchool of Physics, Jilin Normal University, Siping, 136000, P. R. China

† Electronic supplementary information (ESI) available: supplementary figures and digital photographs of all nanoparticles, the XRD pattern of the middle state sample 1 in the reduced process, the FTIR spectrum of the $\alpha\text{-Fe}_2\text{O}_3$, Fe_3O_4 and $\gamma\text{-Fe}_2\text{O}_3$ nanoparticles in the region of 200 to 400 cm⁻¹. See DOI: 10.1039/c3ce41269e

The mechanism and conditions for the phase transformations from $\alpha\text{-Fe}_2\text{O}_3$ to Fe_3O_4 and Fe_3O_4 to $\gamma\text{-Fe}_2\text{O}_3$ nanoparticles have been investigated by the thermal analysis method. The morphologies and structures of various nanoparticles after annealing in H₂ : Ar at 294 °C and in an O₂ atmosphere at 302 °C have been examined and characterized. Finally, we confirmed that the monodisperse, porous and magnetic $\gamma\text{-Fe}_2\text{O}_3$ nanoparticles could be obtained by annealing the $\alpha\text{-Fe}_2\text{O}_3$ nanoparticles synthesized by the hydrothermal route.

Although the morphologies of the $\alpha\text{-Fe}_2\text{O}_3$ nanoparticles were very rich, the spindle $\alpha\text{-Fe}_2\text{O}_3$ nanoparticles from iron(III) perchlorate were prepared by the hydrothermal synthesis, which has some advantages, due to their smaller sizes and higher axial ratio than that from the typical iron source (*i.e.* FeCl₃, Fe(NO₃)₃).¹⁷ Herein, the thermal analysis method was used first for investigation of the phase transformation in the $\alpha\text{-Fe}_2\text{O}_3$ nanoparticles. According to the results of thermogravimetric (TG) and differential thermal analysis (DTA), we were able to determine the conditions for the phase transformations in the materials.¹⁸ For this purpose, we studied the morphology and structure changes in the as-prepared samples after the annealing process, trying to find a facile route to fabricate Fe_3O_4 and $\gamma\text{-Fe}_2\text{O}_3$ nanoparticles, which is of great importance for the design and applications of the iron oxide.

All of the chemicals used were of analytical grade purity. No additional purification was provided.

A typical synthesis scheme of the preparation of the monodisperse $\alpha\text{-Fe}_2\text{O}_3$ nanoparticles of a spindle shape was as such: 1.677 g (3 mmol) of iron(III) perchlorate (Fe(ClO₄)₃·xH₂O (Alfa Aesar) were added to 30 mL of deionized water, which resulted in the formation of a transparent yellow solution. After 30 min stirring, 0.018 g of sodium dihydrogen phosphate anhydrous (NaH₂PO₄, Sigma-Aldrich) and 0.18 g of urea ((NH₂)₂CO, Sigma-Aldrich) were added to the solution.

Subsequently, this mixed solution was placed into a 100 mL Teflon-lined autoclave. The autoclave was sealed and the solution was annealed at 120 °C for 12 h. Then, the product was cooled down to room temperature. The precipitates were obtained by separation from their mother solution by centrifugation and washed several times with deionized water

and absolute ethanol. Finally, the red products were dried in air at 60 °C for 4 h. They are denoted as $\alpha\text{-Fe}_2\text{O}_3$ sample (i).

Then the $\alpha\text{-Fe}_2\text{O}_3$ sample was placed into a porcelain boat and heated in a tubular oven in an H₂ : Ar (5% : 95%) mixture at 100 °C for 1 h and, after that, at 200 °C for 1 h. The heating rate was 10 °C min⁻¹. Finally, the sample was treated at 294 °C for 0.5 h. The product obtained is denoted as sample 1.

Then the final treatment was provided for 1 h under the same conditions, which yielded the black product denoted as the Fe₃O₄ sample (ii).

The as-prepared Fe₃O₄ sample (ii) was oxidized in high purity O₂ at 100 °C for 1 h, 200 °C for 1 h and 302 °C for 1 h. The product was named as the $\gamma\text{-Fe}_2\text{O}_3$ sample (iii).

All of the products were cooled in the tubular oven in a natural way. Finally, the obtained samples were collected for measurements and characterizations.

The as-obtained samples were characterized by powder X-ray diffraction (XRD) with a D/max-rB and Cu K α ($\lambda = 1.54178 \text{ \AA}$) used as the radiation source, while the operation voltage and current were maintained at values of 60 kV and 200 mA, respectively.

The size and the morphology of the as-prepared samples were studied by a high resolution transmission electron microscope (HRTEM) TECNAI G² F20 operated at a 100 kV accelerating voltage. The TG-DTA analyses were performed with the help of a ZRY-2P device (Shanghai Instrument Company) in the temperature range from 30 °C to 500 °C (from 30 °C to 400 °C) at three heating rates, namely, 5 °C min⁻¹, 10 °C min⁻¹ and 15 °C min⁻¹ both in H₂ : Ar (5% : 95%) or O₂ gas flow with a rate of 40 mL min⁻¹.

X-ray photoelectron spectroscopy (XPS) spectra were measured by a PHI 5700 ESCA X-ray photoelectron spectrometer using a monochromated Al Ka 200 W X-ray source which provided a pass energy of 200 eV for survey scans and 30 eV for high resolution scans.

Nitrogen adsorption-desorption isotherms were obtained at room temperature (300 K) using an ASAP 2020 (Micromeritics) instrument. Prior to the analysis, the samples were degassed under vacuum at 150 °C for 5 h to evacuate the physically adsorbed moisture. The mean pore diameter and the diameter distribution were calculated from the adsorption branch of the isotherm using the Barrett-Joyner-Halenda (BJH) method. The specific surface area was calculated using the Brunauer-Emmett-Teller (BET) model.

Magnetic measurements were carried out by a vibrating sample magnetometer (VSM, Lake Shore 7407) at room temperature in a maximum field of 15 kOe. The ⁵⁷Fe Mössbauer spectra for the as-prepared samples were investigated by a Mössbauer system (FAST Comtec) at room temperature in a conventional constant acceleration mode using a ⁵⁷Co(Pd) source.

Fig. 1 shows the TG and DTA dependency for the $\alpha\text{-Fe}_2\text{O}_3$ and Fe₃O₄ nanoparticles measured in a H₂ : Ar mixture and O₂ at a heating rate of 10 °C min⁻¹. The TG curve of the $\alpha\text{-Fe}_2\text{O}_3$ nanoparticles exhibits two regions (Fig. 1a). The first range (below 100 °C) illustrates the weight enhancement due to the

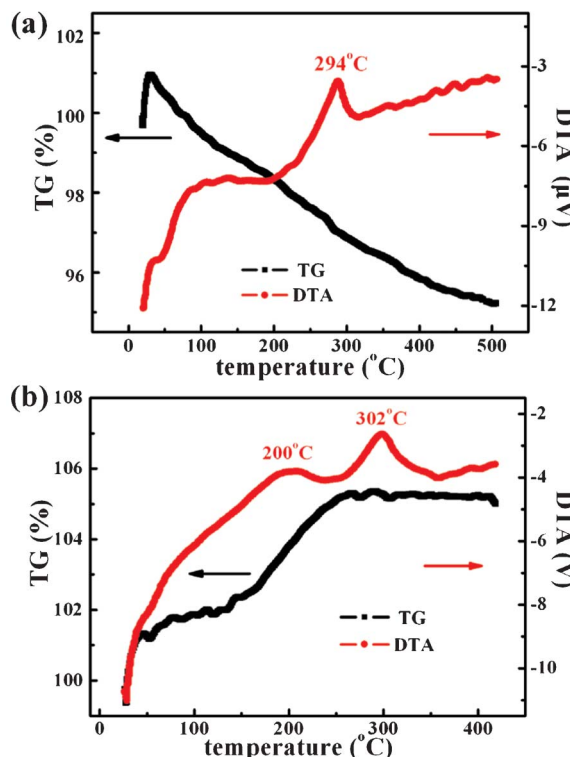


Fig. 1 (a) The TG and DTA dependency for $\alpha\text{-Fe}_2\text{O}_3$ reduced to Fe_3O_4 nanoparticles in $\text{H}_2 : \text{Ar}$ (5% : 95%). (b) The TG and DTA dependency for Fe_3O_4 transformed to $\gamma\text{-Fe}_2\text{O}_3$ nanoparticles in O_2 . All measurements were taken at a heating rate of 10 °C min⁻¹.

adsorption of H₂O molecules formed by the surface reaction between H₂ gas and the oxygen atoms of the iron oxide.¹⁹ The second range (between 150 °C and 350 °C) is characteristic of weight loss. Meanwhile, the DTA curve shows a sharp exothermic peak at 294 °C which is associated with the phase transformation from the $\alpha\text{-Fe}_2\text{O}_3$ to the Fe_3O_4 nanoparticles. In the oxidation, the TG curve also has two ranges (Fig. 1b). The first range illustrates the weight enhancement of the Fe_3O_4 nanoparticles. Since there is no evident thermal effect below 200 °C, this enhancement may be attributed to the adsorption of O₂ gas.²⁰ The second range between 250 °C to 350 °C exhibits a sharp exothermic DTA peak at 302 °C where the oxidation proceeds at the highest rate.²¹ Moreover, the thermal analysis at different heating rates of 5 °C min⁻¹, 10 °C min⁻¹ and 15 °C min⁻¹ was carried out to demonstrate the influence of the heating rate on the annealing process (as Fig. S1–S4, ES[†]).

The TEM photographs are shown in Fig. 2(a)–2(c), which obviously display the morphologies of the as-prepared samples of $\alpha\text{-Fe}_2\text{O}_3$ (i), Fe_3O_4 (ii) and $\gamma\text{-Fe}_2\text{O}_3$ (iii), respectively. The pore sizes of the Fe_3O_4 and $\gamma\text{-Fe}_2\text{O}_3$ nanoparticles are enhanced compared with the original $\alpha\text{-Fe}_2\text{O}_3$ nanoparticles. The results indicate also that the annealing treatment in $\text{H}_2 : \text{Ar}$ and O_2 produces small molecules, *i.e.*, H₂O,²² which lead to a decrease in the grain size of the nanoparticles.²³ Fig. 2(d)–2(f) show the HRTEM images of the edge of an individual nanoparticle

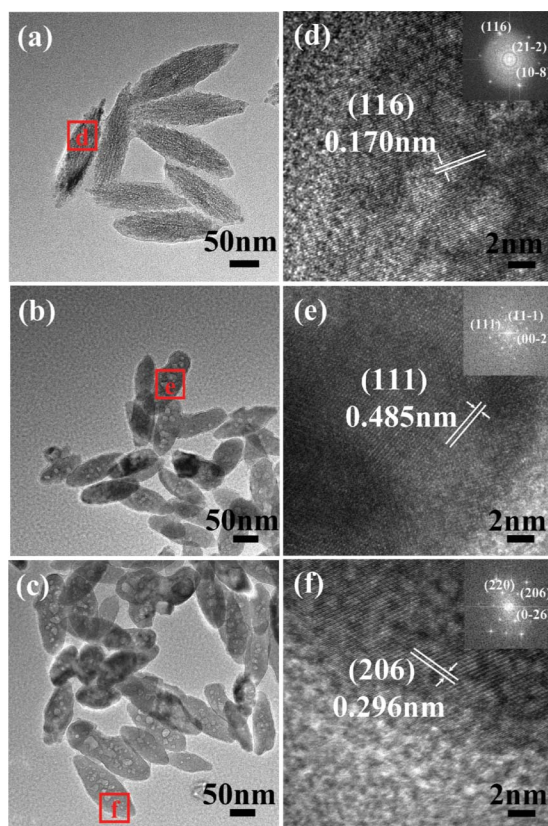


Fig. 2 The TEM photographs of the as-prepared (a) α - Fe_2O_3 , (b) Fe_3O_4 and (c) γ - Fe_2O_3 nanoparticles. The HRTEM details of the edges of an individual (d) α - Fe_2O_3 , (e) Fe_3O_4 and (f) γ - Fe_2O_3 nanoparticle, respectively. The inserts are the FFT patterns of the individual nanoparticle in (d)–(f).

corresponding to Fig. 2(a)–2(c), respectively. Clearly, the interatomic separation of 0.170 nm of the α - Fe_2O_3 nanoparticles is in good agreement with interatomic separation in the (116) plane. After reduction at 294 °C for 1 h, the interatomic separation of 0.485 nm indicates the presence of the (111) plane of the Fe_3O_4 phase, which demonstrates that the phase transformation is completed by the annealing.²⁴ In addition, the distinct interatomic separation of 0.296 nm indicates the (206) plane of our target product, that is the γ - Fe_2O_3 nanoparticles. The inserts of Fig. 2(d)–2(f) are also in good agreement with these conclusions. Moreover, numerous measurements carried out in this work showed that phase transformations between the α - Fe_2O_3 to Fe_3O_4 , and Fe_3O_4 to γ - Fe_2O_3 nanoparticles occur and can be reliably reproduced.

To study the changes in the crystalline structures, the XRD patterns of all of the as-prepared samples and reference patterns are presented in Fig. 3. Obviously, all of the peaks of the as-prepared α - Fe_2O_3 sample in Fig. 3(i) are in good agreement with the reference data for the α - Fe_2O_3 phase (JCPDS card 33-0664), as shown in Fig. 3(iv). No additional peaks belonging to other iron oxide phases were observed, which indicates the good crystallinity and high purity of the original α - Fe_2O_3 nanoparticles. For the as-prepared Fe_3O_4 sample after reduction for 1 h, the diffraction peaks are in

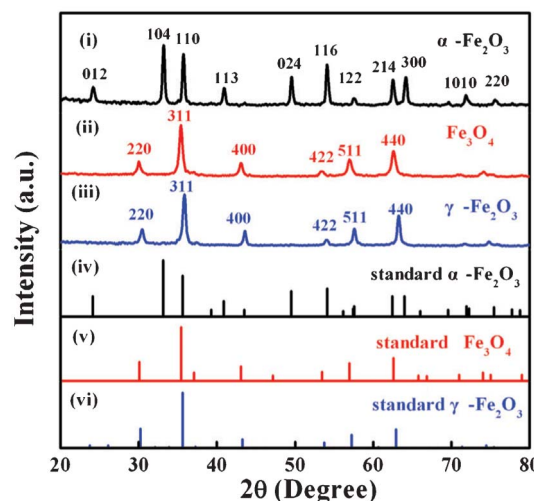


Fig. 3 The XRD patterns of the as-prepared (i) α - Fe_2O_3 , (ii) Fe_3O_4 and (iii) γ - Fe_2O_3 nanoparticles. The standard patterns of (iv) α - Fe_2O_3 (JCPDS card 33-0664), (v) Fe_3O_4 (JCPDS card 65-3107) and (vi) γ - Fe_2O_3 (JCPDS card 39-1356) are also shown for comparison.

good agreement with the data for the cubic spinel structured Fe_3O_4 (JCPDS card 65-3107), except for sample 1 (as Fig. S5 in ESI†) which presents itself as the mixture of the α - Fe_2O_3 and Fe_3O_4 phases. The d -spacing of 2.532 ± 0.001 Å calculated by Bragg's formula corresponds to the most intensive peak of (311) at 35.42° , which shows that the phase transformation is completed by this reducing process. For the as-prepared γ - Fe_2O_3 sample after oxidation in O_2 for 1 h, the XRD patterns are in good coincidence with the reference data for the cubic close packed γ - Fe_2O_3 phase (JCPDS card 39-1356). Herein, the 2.502 ± 0.001 Å d -spacing corresponds to the (311) peak at 35.86° . This result demonstrated that this oxidation method is highly efficient for the phase transformation between the Fe_3O_4 and γ - Fe_2O_3 phases.

Furthermore, the changes in the surface structures of the samples are confirmed by the XPS spectra, shown in Fig. 4(a)–4(c). Fig. 4(a) shows the $\text{Fe } 2p_{3/2}$ peak at 710.8 eV and the $\text{Fe } 2p_{1/2}$ peak at 723.6 eV for α - Fe_2O_3 . Compared with the γ - Fe_2O_3 sample in Fig. 4(c), the $\text{Fe } 2p_{3/2}$ peak at 710.35 eV and the $\text{Fe } 2p_{1/2}$ peak 724.0 eV are similar to each other. However, the satellite peak at 715.6 eV is assigned to the surface peak of the α - Fe_2O_3 nanoparticles, which is different to the γ - Fe_2O_3 phase.²⁵ The $\text{Fe } 2p$ peaks of the Fe_3O_4 sample are shown in Fig. 4(b). The peaks at 710.6 and 724.2 eV are assigned to the $\text{Fe}-\text{O}$ bond of the Fe^{2+} ion and the other two peaks at 713.2 and 726.8 eV are assigned to the $\text{Fe}-\text{O}$ bond of the Fe^{3+} ion.²⁶ It is also confirmed that the Fe^{2+} ion is effectively formed by the annealing at 294 °C in the $\text{H}_2 : \text{Ar}$ mixture. Considering together the XRD patterns and the XPS spectra, one may conclude that the reduction and the oxidation treatment provide the successful transformations between the α - Fe_2O_3 and Fe_3O_4 phases, as well as between the Fe_3O_4 and γ - Fe_2O_3 phases.

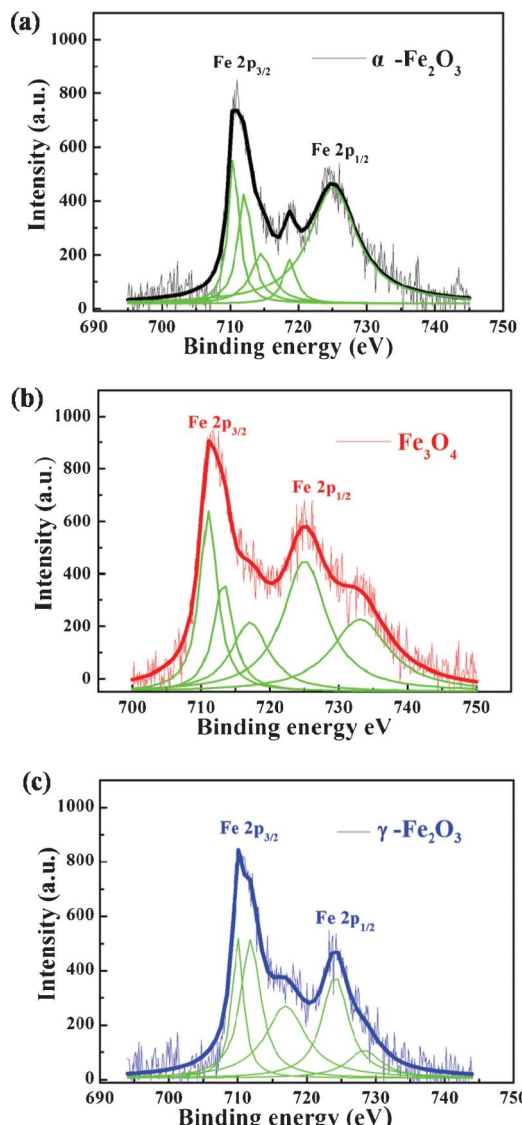


Fig. 4 The XPS spectrum for the Fe 2p peaks of the (a) $\alpha\text{-Fe}_2\text{O}_3$, (b) Fe_3O_4 and (c) $\gamma\text{-Fe}_2\text{O}_3$ nanoparticles.

Raman spectra are used to identify the iron oxide phases in the $\alpha\text{-Fe}_2\text{O}_3$, Fe_3O_4 and $\gamma\text{-Fe}_2\text{O}_3$ nanoparticles (Fig. 5(a)). The spectra are very similar to those of the reference data for the standard powders.²⁷ However, the peak positions are shifted to higher frequencies by $3\text{--}5\text{ cm}^{-1}$ due to the quantum size effect.²⁸ The Raman shift values are presented in Table 1. The Raman spectrum of the as-prepared $\alpha\text{-Fe}_2\text{O}_3$ nanoparticles does not contain the peaks belonging to the other two iron oxides, Fe_3O_4 and $\gamma\text{-Fe}_2\text{O}_3$. The peaks at 221 and 497 cm^{-1} are assigned to A1g modes²⁹ whereas the peaks at 244 , 292 , 406 and 611 cm^{-1} are assigned to Eg modes. The peaks in the Fe_3O_4 nanoparticle spectrum at 305 and 534 cm^{-1} are reliably assigned to the T2g mode, whereas the peak at 513 cm^{-1} is assigned to the Eg mode and the peak at 660 cm^{-1} is assigned to the A1g mode. The spectra prove that the transformation between $\alpha\text{-Fe}_2\text{O}_3$ to Fe_3O_4 nanoparticles was carried out

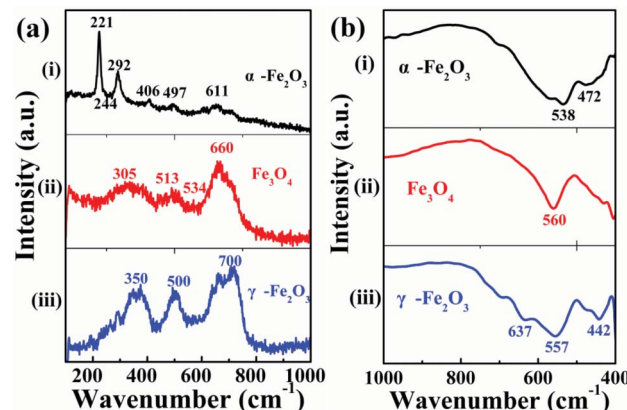


Fig. 5 (a) The Raman spectra of the as-prepared (i) $\alpha\text{-Fe}_2\text{O}_3$, (ii) Fe_3O_4 and (iii) $\gamma\text{-Fe}_2\text{O}_3$ nanoparticles. The laser wave length was 533 nm . (b) The FTIR spectra of the as-prepared (i) $\alpha\text{-Fe}_2\text{O}_3$, (ii) Fe_3O_4 and (iii) $\gamma\text{-Fe}_2\text{O}_3$ nanoparticles.

completely. For the as-prepared $\gamma\text{-Fe}_2\text{O}_3$ nanoparticles, the peaks at 350 , 500 and 700 cm^{-1} are assigned to the T2g, T2g and A1g modes, respectively, which shows that the oxidation of the Fe_3O_4 nanoparticles was highly efficient and complete.

The samples were investigated also by a FTIR spectroscopy, which is shown in Fig. 5b. The $\alpha\text{-Fe}_2\text{O}_3$ nanoparticle spectrum shows characteristic peaks at 538 cm^{-1} and 472 cm^{-1} , which are attributed to vibrations of the Fe–O functional groups. There are five peaks in the region of $200\text{--}400\text{ cm}^{-1}$, which are attributed to the Eu and A2u infrared-active modes (as seen in Fig. S6 in the ESI†).³⁰ The Fe_3O_4 spectrum has only a single absorption peak at 560 cm^{-1} in the region of $1000\text{--}400\text{ cm}^{-1}$ as has been reported elsewhere.³¹ Furthermore, three peaks for the T1u modes are presented in the FTIR region of $200\text{--}400\text{ cm}^{-1}$ (as seen in Fig. S7 in the ESI†), where these peaks are assigned to its orthorhombic phase. In the $\gamma\text{-Fe}_2\text{O}_3$ spectrum, the IR absorption peak at 637 cm^{-1} , 557 cm^{-1} and 442 cm^{-1} are assigned to the Fe–O stretching vibration. Obvious peaks in the region of 395 to 440 cm^{-1} are also attributed the T2 infrared-active modes in (as seen in Fig. S8 in the ESI†).³² The series of experiments carried out by XRD, XPS and Raman spectroscopy excellently confirmed that phase transformations between $\alpha\text{-Fe}_2\text{O}_3$ and Fe_3O_4 due to the treatment at $294\text{ }^\circ\text{C}$ for 1 hour, and between Fe_3O_4 and the $\gamma\text{-Fe}_2\text{O}_3$ by the treatment at $302\text{ }^\circ\text{C}$ for 1 hour were achieved successfully.

A most effective method used to identify iron oxides, including the $\alpha\text{-Fe}_2\text{O}_3$, Fe_3O_4 and $\gamma\text{-Fe}_2\text{O}_3$ nanoparticles, is Mössbauer spectroscopy. Fig. 6 shows the Mössbauer spectra

Table 1 The Raman active modes of the as-prepared $\alpha\text{-Fe}_2\text{O}_3$, Fe_3O_4 and $\gamma\text{-Fe}_2\text{O}_3$ nanoparticles

Sample	Raman shift (cm^{-1}) and assignment			
$\alpha\text{-Fe}_2\text{O}_3$	221 (A1g)	244 (Eg)	292 (Eg)	406 (Eg)
	497 (A1g)	611 (Eg)		
Fe_3O_4	305 (T2g)	513 (Eg)	534 (T2g)	660 (A1g)
$\gamma\text{-Fe}_2\text{O}_3$	350 (T2g)	500 (T2g)	700 (A1g)	

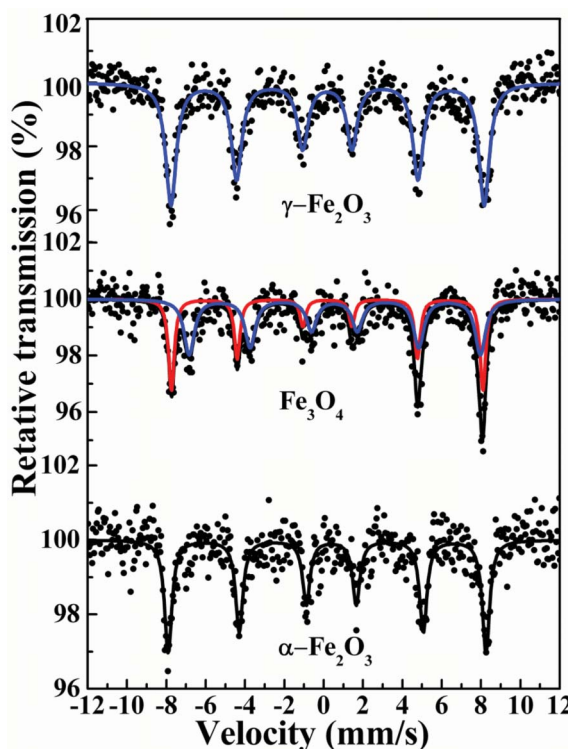


Fig. 6 The Mössbauer spectra of the as-prepared α - Fe_2O_3 , Fe_3O_4 and γ - Fe_2O_3 nanoparticles.

for all of the as-prepared samples. The isomer shift (IS) and velocity are given relative to those for α -Fe at room temperature. The Mössbauer spectra are fitted with Lorentzian curves using the least square method (the calculated parameters are given in Table 2). For the original α - Fe_2O_3 nanoparticles, the sextet with hyperfine magnetic splitting is of 500.8 ± 0.1 kOe. This result confirms the high purity and quality of the α - Fe_2O_3 particles.³³ After annealing at 294°C in H_2 , the sextets with hyperfine magnetic splittings of 490.8 and 459.0 ± 0.1 kOe are presented in the as-prepared Fe_3O_4 nanoparticles, which correspond to the A and B sites of the reference Fe_3O_4 .³⁴ This implies that the α - $\text{Fe}_2\text{O}_3 \rightarrow \text{Fe}_3\text{O}_4$ conversion yields the contents of the A and B sites to be 42.4% and 57.6 ± 0.1 , respectively. The transformation efficiency nearly reaches 100% . The terminal product (γ - Fe_2O_3) has the sextet with a hyperfine magnetic splitting of 493.7 ± 0.1 kOe which is in agreement with the reported data concerning the

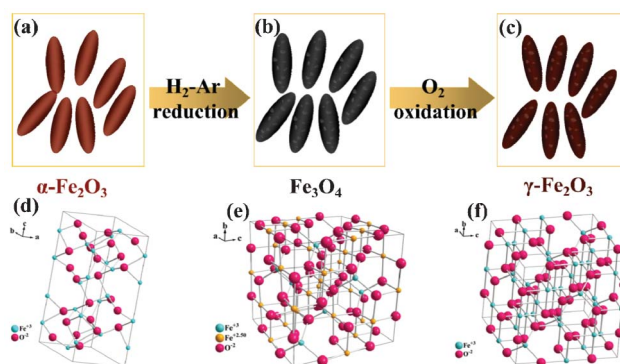


Fig. 7 A schematic illustration of the phase transformation for the (a) α - Fe_2O_3 , (b) Fe_3O_4 and (c) γ - Fe_2O_3 nanoparticles under reduction and oxidation processes. (d)–(f) The three-dimensional crystal structures of the α - Fe_2O_3 , Fe_3O_4 and γ - Fe_2O_3 nanoparticles, respectively.

γ - Fe_2O_3 nanoparticles.³⁵ The lower value is explained by the size-dependent effects and by the defects of the nanoparticles. Therefore, it is believed that the phase transformations between the α - Fe_2O_3 and Fe_3O_4 state and the Fe_3O_4 and γ - Fe_2O_3 state are facile, highly efficient and have good atom economics.

Fig. 7 demonstrates the scheme of the phase transformations. The reduction was carried out at 294°C for 1 hour, which led to the α - Fe_2O_3 (a) \rightarrow Fe_3O_4 (b) phase transformation. The oxidizing process took place at 302°C for 1 hour causing the Fe_3O_4 (b) \rightarrow γ - Fe_2O_3 (c) phase transformation. The annealing processes are according to the results for the thermal analysis. The exothermic peaks in the curves of DTA are related to the highest rate of the reduction and oxidation. The crystal structures of the α - Fe_2O_3 , Fe_3O_4 and γ - Fe_2O_3 nanoparticles are shown in Fig. 7(d) and 7(e). The α - Fe_2O_3 has a rhombohedrally centered hexagonal structure and which is related to the $R\bar{3}c$ space group. The α - $\text{Fe}_2\text{O}_3 \rightarrow \text{Fe}_3\text{O}_4$ transformation is accompanied by the change from a hexagonal close-packed oxide ion array (α - Fe_2O_3) to a cubic close-packed array (Fe_3O_4). The reduction may produce micro-pores in the as-prepared Fe_3O_4 nanoparticles.³⁶ As well as Fe_3O_4 of the $Fd\bar{3}m$ space group, γ - Fe_2O_3 possesses a cubic crystal structure of an inverse spinel type, which has two nonequivalent crystallographic sites, *i.e.*, the tetrahedral and octahedral sites. Due to the similarity of the structures, the phase transformations could easily be achieved under soft conditions in an oxidation atmosphere.

Table 2 The high fine parameters of the fitted curves to the Mössbauer spectra of the α - Fe_2O_3 , Fe_3O_4 and γ - Fe_2O_3 nanoparticles^a

Component	IS (mm s ⁻¹) (± 0.001)	QS (mm s ⁻¹) (± 0.001)	Hf (kOe) (± 0.1)	WHWM (mm s ⁻¹) (± 0.001)	AREA (%) (± 0.1)
α - Fe_2O_3	0.387	0.211	500.8	0.224	100
Fe_3O_4	A 0.288	0.011	490.8	0.175	42.4
	B 0.661	0.022	459.0	0.315	57.6
γ - Fe_2O_3	0.299	0.015	493.7	0.325	100

^a Where IS is the isomer shift relative to α -Fe at room temperature. QS is the quadrupole shift. Hf is the magnetic hyperfine field at ^{57}Fe nuclei. WHWM is the half maximum linewidth. AREA is the area of the spectrum component.

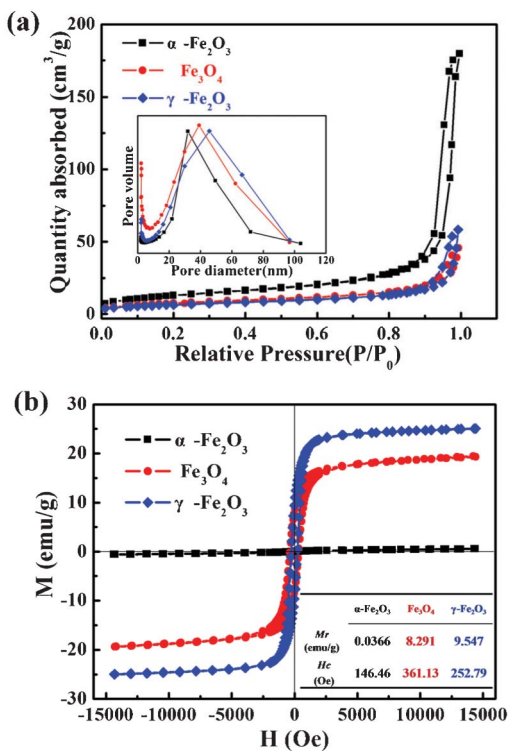


Fig. 8 (a) The nitrogen adsorption and desorption isotherms and pore size distribution curves (inset) calculated by the BJH formula for the as-prepared α -Fe₂O₃ (black line), Fe₃O₄ (red line) and γ -Fe₂O₃ (blue line) nanoparticles. (b) The magnetic hysteresis loops measured at room temperature for the as-prepared α -Fe₂O₃, Fe₃O₄ and γ -Fe₂O₃ nanoparticles.

To estimate the pore size and the specific surface area, the Brunauer–Emmett–Teller (BET) nitrogen adsorption and desorption isotherms and the pore size distribution curves of the as-products are presented in Fig. 8(a). It was determined that the specific surface areas of the α -Fe₂O₃, Fe₃O₄ and γ -Fe₂O₃ are 74.11 m² g⁻¹, 45.07 m² g⁻¹ and 38.51 m² g⁻¹, respectively. The average pore diameter for the α -Fe₂O₃ sample was 30 nm whereas the pore volume was 0.1453 cm³ g⁻¹. For Fe₃O₄, the pore diameter was 39 nm and the pore volume was 0.0439 cm³ g⁻¹, correspondingly, and for the γ -Fe₂O₃ the values were 45 nm and 0.0447 cm³ g⁻¹. These data show that the thermal treatment enhances the pore size and number, which is attributed to the fact that the α -Fe₂O₃ nanoparticles possess a comparatively compact structure. However, the Fe₃O₄ and γ -Fe₂O₃ nanoparticles being annealed form the defect crystal structures with the pores.^{37,38}

The magnetic hysteresis measurements of the samples of the α -Fe₂O₃, Fe₃O₄ and γ -Fe₂O₃ nanoparticles were carried out at room temperature in the magnetic field sweeping from -15 kOe to 15 kOe. The magnetic hysteresis (M - H) curves are displayed in Fig. 8(b), respectively, which indicate that the samples have a ferrimagnetic behaviour.³⁹ The insert table in Fig. 8(b) shows the values of the residual magnetization (M_r) and coercive force (H_c) for the three phases. It is easy to find that the M_r and H_c values for the Fe₃O₄ and γ -Fe₂O₃

nanoparticles are much higher than that for the α -Fe₂O₃ nanoparticles. In addition, the comparison of the M_r and H_c value for the Fe₃O₄ and γ -Fe₂O₃ nanoparticles obviously displays that the H_c value for the Fe₃O₄ nanoparticles is higher than those for the γ -Fe₂O₃ nanoparticles, although, the M_r value for the Fe₃O₄ nanoparticles was lower than that for the γ -Fe₂O₃ nanoparticles. These results are attributed to the differences in the crystallinity,⁴⁰ free surface, grain boundaries⁴¹ and surface defects⁴² for the as-prepared nanoparticles and for the treated ones by reduction and oxidation. The phase transformation of the Fe₂O₃ nanoparticles also improves the magnetic properties (as Fig. S9 in ESIT), which are valuable for applications in drug delivery, bioseparation, and so on.

In conclusion, α -Fe₂O₃ nanoparticles prepared by a facile hydrothermal route were thermally reduced to Fe₃O₄ nanoparticles in a H₂ : Ar mixture and were consequently transformed to γ -Fe₂O₃ nanoparticles by heat treatment in O₂. The appropriate conditions were: 294 °C for the reduction and 302 °C for the oxidation at the heating rate of 10 °C min⁻¹. The structures, examined by TEM, XRD, XPS, FTIR and Raman and Mössbauer spectroscopy, demonstrated the appearance of the Fe₃O₄ and γ -Fe₂O₃ nanoparticles. Furthermore, these results determined that the reduction treatment should be carried out at 294 °C in the H₂ : Ar mixture for the α -Fe₂O₃ → the Fe₃O₄ phase transformation and the oxidation treatment should be carried out at 302 °C in O₂ for the Fe₃O₄ → γ -Fe₂O₃ phase transformation. The BET test showed that the pore sizes in the γ -Fe₂O₃ nanoparticles were enhanced compared with those in the original α -Fe₂O₃ nanoparticles. Finally, the magnetic properties display that the M_r and H_c values for the Fe₃O₄ and γ -Fe₂O₃ nanoparticles are higher than those for the α -Fe₂O₃ nanoparticles, which supplies an enhanced magnetic route by phase transformations and paves the ways for novel applications of the α -Fe₂O₃ nanoparticles in magnetic design and functional materials.

We thank the National Natural Science Foundation of China (No. 51010005, 91216123, 51174063), the program for New Century Excellent Talents in University (NCET-08-0168). Natural Science Funds for Distinguished Young Scholar of Heilongjiang Province. The project of International Cooperation supported by Ministry of Science and Technology of China.

Notes and references

- Y. L. Chueh, M. W. Lai, J. Q. Liang, L. J. Chou and Z. L. Wang, *Adv. Funct. Mater.*, 2006, **16**, 2243.
- P. P. Yang, S. L. Gai and J. Lin, *Chem. Soc. Rev.*, 2012, **41**, 3679.
- X. L. Mou, X. J. Wei, Y. Li and W. J. Shen, *CrystEngComm*, 2012, **14**, 5107.
- J. S. Xu and Y. J. Zhu, *ACS Appl. Mater. Interfaces*, 2012, **4**, 4752.
- C. T. Yavuz, J. T. Mayo, W. W. Yu, A. Prakash, J. C. Falkner, S. Yean, L. Cong, H. J. Shipley, A. Kan, M. Tomson, D. Natelson and V. L. Colvin, *Science*, 2006, **314**, 964.

- 6 S. Si, C. Li, X. Wang, D. Yu, Q. Peng and Y. Li, *Cryst. Growth Des.*, 2005, **5**, 391.
- 7 H. L. Zhu, D. R. Yang, L. M. Zhu, H. Yang, D. L. Jin and K. H. Yao, *J. Mater. Sci.*, 2007, **42**, 9205.
- 8 Y. E. Mendili, J. F. Bardeau, N. Randrianantoandro, F. Grasset and J. Grueneche, *J. Phys. Chem. C*, 2012, **116**, 23785.
- 9 Q. L. Peng, Y. Zhang, F. Shi and Y. Q. Deng, *Chem. Commun.*, 2011, **47**, 6476.
- 10 B. L. Lv, Y. Xu, D. Wu and Y. H. Sun, *CrystEngComm*, 2011, **13**, 7293.
- 11 C. Q. Hu, Z. H. Gao and X. R. Yang, *Mater. Chem. Phys.*, 2007, **104**, 429.
- 12 C. J. Jia, L. D. Sun, Z. G. Yan, L. P. You, F. Luo, X. D. Han, Y. C. Pang, Z. Zhang and C. H. Yan, *Angew. Chem., Int. Ed.*, 2005, **44**, 4328.
- 13 C. T. Liu, J. Ma and H. Y. Chen, *RSC Adv.*, 2012, **2**, 1009.
- 14 X. H. Guo, S. L. Zhong, J. Zhang, W. Wang, J. J. Mao and G. Xie, *J. Mater. Sci.*, 2010, **45**, 6467.
- 15 G. K. Pradhan and K. M. Parida, *ACS Appl. Mater. Interfaces*, 2011, **3**, 317.
- 16 S. Bharathi, D. Nataraj, M. Seetha, D. Mangalaraj, N. Ponpandian, Y. Masuda, K. Senthil and K. Yong, *CrystEngComm*, 2010, **12**, 373.
- 17 F. Jiao, J. C. Jumas, M. Womes, A. V. Chadwick, A. Harrison and P. G. Bruce, *J. Am. Chem. Soc.*, 2006, **128**, 12905.
- 18 Y. A. Niu, J. P. Zhao, X. Zhang, X. J. Wang, J. Wu, Y. Li and Y. Li, *Appl. Phys. Lett.*, 2012, **101**, 181903.
- 19 H. H. Dong, M. J. Xie, J. Xu, M. F. Li, L. M. Peng, X. F. Guo and W. P. Ding, *Chem. Commun.*, 2011, **47**, 4019.
- 20 Z. Y. Cai, H. J. Zhou, J. Song, F. Zhao and J. S. Li, *Dalton Trans.*, 2011, **40**, 8335.
- 21 W. Q. Peng, Z. M. Wang, N. Yoshizawa, H. Hatori, T. Hirotsub and K. Miyazawac, *J. Mater. Chem.*, 2010, **20**, 2424.
- 22 W. Wu, S. F. Zhang, X. H. Xiao, J. Zhou, F. Ren, L. L. Sun and C. Z. Jiang, *ACS Appl. Mater. Interfaces*, 2012, **4**, 3602.
- 23 X. N. Xu, Y. Wolfus, A. Shaulov, Y. Yeshurun, I. Felner, I. Nowik, Yu. Koltypin and A. Gedanken, *J. Appl. Phys.*, 2002, **91**, 4611.
- 24 R. G. Shi, X. H. Liu, G. H. Gao, R. Yi and G. Z. Qiu, *J. Alloys Compd.*, 2009, **485**, 548.
- 25 S. Bharathi, D. Nataraj, M. Seetha, D. Mangalaraj, N. Ponpandian, Y. Masuda, K. Senthil and K. Yong, *CrystEngComm*, 2010, **12**, 373.
- 26 R. Dedryvere, M. Maccario, L. Croguennec, F. L. Cras, C. Delmas and D. Gonbeau, *Chem. Mater.*, 2008, **20**, 7164.
- 27 D. L. A. De Faria, S. V. Silva and M. T. De Oliveira, *J. Raman Spectrosc.*, 1997, **28**, 873.
- 28 C. H. Kim, H. J. Chun, D. S. Kim, S. Y. Kim, J. Park, J. Y. Moon, G. Lee, J. Yoon, Y. Jo, M. H. Jung, S. I. Jung and C. J. Lee, *Appl. Phys. Lett.*, 2006, **89**, 223103.
- 29 A. M. Jubb and H. C. Allen, *ACS Appl. Mater. Interfaces*, 2010, **2**, 2804–2812.
- 30 I. Chamritski and G. Burns, *J. Phys. Chem. B*, 2005, **109**, 4965.
- 31 N. Du, Y. F. Xu, H. Zhang, C. X. Zhai and D. R. Yang, *Nanoscale Res. Lett.*, 2010, **5**, 1295.
- 32 E. Wolska, W. Szajda and P. Piszcza, *Mater. Lett.*, 1994, **21**, 191.
- 33 Y. F. Krupyansky and I. P. Suzdalev, *Sov. Phys. JETP.*, 1974, **38**, 859.
- 34 I. S. Lyubutin, C. R. Lin, Yu. V. Korzhetskiy, T. V. Dmitrieva and R. K. Chiang, *J. Appl. Phys.*, 2009, **106**, 034311.
- 35 C. J. Cheng, C. C. Lin, R. K. Chiang, C. R. Lin, I. S. Lyubutin, E. A. Alkaev and H. Y. Lai, *Cryst. Growth Des.*, 2008, **8**, 877.
- 36 L. Machala, J. Tucek and R. Zboril, *Chem. Mater.*, 2011, **23**, 3255.
- 37 D. H. Chen, X. L. Jiao and D. R. Chen, *Mater. Res. Bull.*, 2001, **36**, 1057–1064.
- 38 Y. J. Chen, G. Xiao, T. S. Wang, Q. Y. Ouyang, L. H. Qi, Y. Ma, P. Gao, C. L. Zhu, M. S. Cao and H. B. Jin, *J. Phys. Chem. C*, 2011, **115**, 13603.
- 39 Q. Zhang, S. J. Liu and S. H. Yu, *J. Mater. Chem.*, 2009, **19**, 191.
- 40 X. Zhang, Y. A. Niu, Y. Li, X. M. Hou, Y. B. Wang, R. Bai and J. P. Zhao, *Mater. Lett.*, 2013, **99**, 111.
- 41 G. B. Sun, B. X. Dong, M. H. Cao, B. Q. Wei and C. W. Hu, *Chem. Mater.*, 2011, **23**, 1587.
- 42 Q. Zhang, S. J. Liu and S. H. Yu, *J. Mater. Chem.*, 2009, **19**, 191.